

Article

Low-Temperature Spark Plasma Sintering of $\text{ZrW}_{2-x}\text{Mo}_x\text{O}_8$ Exhibiting Controllable Negative Thermal Expansion

Hui Wei ^{1,*} , Marin Hasegawa ¹, Shunsuke Mizutani ¹, Akihisa Aimi ², Kenjiro Fujimoto ² and Keishi Nishio ¹

¹ Department of Materials Science and Technology, Tokyo University of Science, Tokyo 1258585, Japan; mcdefgahcm@gmail.com (M.H.); yoku_rkz@yahoo.co.jp (S.M.); k-nishio@rs.noda.tus.ac.jp (K.N.)

² Department of Pure and Applied Chemistry, Tokyo University of Science, Chiba 2788510, Japan; akihisa.aimi@rs.tus.ac.jp (A.A.); fujimoto_kenjiro@rs.tus.ac.jp (K.F.)

* Correspondence: 8216701@ed.tus.ac.jp; Tel.: +81-90-9815-7888

Received: 20 August 2018; Accepted: 29 August 2018; Published: 1 September 2018



Abstract: Molybdenum-doped zirconium tungstate ($\text{ZrW}_{2-x}\text{Mo}_x\text{O}_8$) has been widely studied because of its large isotropic coefficient of negative thermal expansion (NTE). However, low density and poor sinterability limit its production and application. In this study, relative density greater than 90% single-phase $\text{ZrW}_{2-x}\text{Mo}_x\text{O}_8$ ($0.0 \leq x \leq 1.0$) sintered bodies were fabricated by spark plasma sintering (500–600 °C for 10 min) using $\text{ZrW}_{2-x}\text{Mo}_x\text{O}_7(\text{OH})_2 \cdot 2\text{H}_2\text{O}$ precursor powders as the starting material. High-temperature X-ray diffraction and thermomechanical analysis were used to investigate the change in the order–disorder phase transition temperature of the sintered materials; it gradually dropped from 170 °C at $x = 0.0$ to 78 °C at $x = 0.5$, and then to below room temperature at $x \geq 0.7$. In addition, all sintered bodies exhibited NTE behavior. The NTE coefficient was controllable by changing the x value as follows: from $-7.85 \times 10^{-6} \text{ °C}^{-1}$ ($x = 0$) to $-9.01 \times 10^{-6} \text{ °C}^{-1}$ ($x = 0.6$) and from $-3.22 \times 10^{-6} \text{ °C}^{-1}$ ($x = 0$) to $-2.50 \times 10^{-6} \text{ °C}^{-1}$ ($x = 1.0$) before and after the phase transition, respectively. Rietveld structure refinement results indicate that the change in the NTE coefficient can be straightforwardly traced to the thermodynamic instability of the terminal oxygen atoms, which only have one coordination.

Keywords: $\text{ZrW}_{2-x}\text{Mo}_x\text{O}_8$; spark plasma sintering; dense sintered body; thermal analysis; negative thermal expansion

1. Introduction

Negative thermal expansion (NTE) materials, which exhibit volume contraction upon warming, have been extensively investigated because of their potential utility in many fields, especially in those requiring precisely controllable negative, positive, or near-zero coefficients of thermal expansion composites [1–6]. A series of NTE materials, including the AM_2O_7 , AM_2O_8 , and $\text{A}_2\text{M}_3\text{O}_{12}$ families have been investigated [7–19]. Among these families, the most representative material is ZrW_2O_8 , which is widely known for its large NTE coefficient ($-4.9 \times 10^{-6} \text{ °C}^{-1}$ to $-8.8 \times 10^{-6} \text{ °C}^{-1}$) over a wide temperature range (-271 °C to 777 °C) and its three-dimensional isotropic (cubic crystal) structure [7,8]. The NTE mechanism of this material is still being discussed; the rigid unit mode (RUM) model proposed by Evans et al. is the most widely accepted [8,9]. The basic model for the NTE mechanism is based on the idea that the rotation of linked polyhedra pull them in toward each other. This motion is seen more locally as the flexing of the Zr–O–W linkage through transverse motions of the O atoms without significant stretching of the Zr–O and W–O bonds.

Another special thermal property of ZrW_2O_8 is its order–disorder phase transition; the change from a low-temperature thermally stable cubic phase ($\alpha\text{-ZrW}_2\text{O}_8$, space group: $P 2_1 3$) to a high-temperature one ($\beta\text{-ZrW}_2\text{O}_8$, space group: $P a \bar{3}$) at around 170 °C. This nearly halves the NTE coefficient, from $-8.8 \times 10^{-6} \text{ }^\circ\text{C}^{-1}$ to $-4.9 \times 10^{-6} \text{ }^\circ\text{C}^{-1}$ [8]. This abrupt change in the coefficient is a disadvantage in practical applications if the phase transition temperature of the material is within the working temperature range. Previous studies found that the reason for this phase transition is related to the breaking of the free $\text{W-O}_{\text{terminal}}$ bonds (terminal oxygen atoms have only one coordination) in the framework structure. In this sense, it is clear that substitution of the W^{6+} cation within the crystal structure by another cation strongly affects the phase transition temperature. Because Mo^{6+} and W^{6+} have the same coordination number and the values of the ionic radius and electronegativity are very close, the phase transition temperature of ZrW_2O_8 can be adjusted by partially doping Mo^{6+} in W^{6+} . Several studies have shown that increasing Mo substitution in $\text{ZrW}_{2-x}\text{Mo}_x\text{O}_8$ leads to a lower phase transition temperature [11,20–23]. Evans et al. reported that the phase transition temperature shifted to below room temperature when $x = 1$, meaning that the discontinuity of NTE is effectively removed at ambient temperature [11,20].

The vast majority of research using X-ray diffraction analysis and the differential scanning calorimetry method to determine the NTE coefficient and the phase transition temperature of $\text{ZrW}_{2-x}\text{Mo}_x\text{O}_8$ powders. However, there was little research about the fabrication of $\text{ZrW}_{2-x}\text{Mo}_x\text{O}_8$ sintered bodies and evaluation of its thermal expansion properties. In terms of application, the fabrication of $\text{ZrW}_{2-x}\text{Mo}_x\text{O}_8$ sintered bodies and the control of their thermal expansion properties are particularly important.

To our knowledge, it is difficult to obtain a pure, dense sintered body using a high-temperature solid-phase method because of the poor sinterability and high-temperature thermodynamically metastable property of $\text{ZrW}_{2-x}\text{Mo}_x\text{O}_8$. We succeeded in fabricating undoped ZrW_2O_8 sintered bodies with a relative density of 95% by spark plasma sintering (SPS) at a relatively low-temperature (600 °C) [24].

In this paper, we describe the fabrication of dense, pure $\text{ZrW}_{2-x}\text{Mo}_x\text{O}_8$ ($0.0 \leq x \leq 1.0$) sintered bodies and the effect of Mo substitution for W on the phase transition temperature and NTE coefficients.

2. Materials and Methods

The $\text{ZrW}_{2-x}\text{Mo}_x\text{O}_8$ sintered bodies were fabricated by SPS using $\text{ZrW}_{2-x}\text{Mo}_x\text{O}_7(\text{OH})_2 \cdot 2\text{H}_2\text{O}$ precursor powders as the starting material. The precursor powders were prepared by a sol-gel method combined with a hydrothermal process. $\text{ZrOCl}_2 \cdot 8\text{H}_2\text{O}$ (Kishida Chemical, Osaka, Japan, 99%) was dissolved in a mixture solvent consisting of 4 mol/L acetic acid and 2-butanol in air. WCl_6 (Kojundo Chemical, Saitama, Japan, 99.99%) and MoCl_5 (Sigma Aldrich, St. Louis, MO, USA, 95%) were dissolved in ethanol in accordance with the stoichiometric ratio of $\text{W}/\text{Mo} = (2 - x):x$ ($x = 0.0, 0.2, 0.5, 0.6, 0.7, 1.0$) in a nitrogen atmosphere, and these solutions were mixed and stirred. The mixed solution of W and Mo was poured into the Zr solution and then stirred for 72 h at room temperature. The dry gel powders (sol-gel precursor powders) were prepared by heating the mixed solution of W, Mo, and Zr at 80 °C in the silicone oil bath. In order to improve the crystallinity of the sol-gel precursor powders, the dry gel powders were dispersed in distilled water, placed in a Teflon-lined Parr bomb, and heated with a mantle heater at 180 °C for 18 h. The synthesized powders were dried in an oven at 60 °C, producing a crystalline $\text{ZrW}_{2-x}\text{Mo}_x\text{O}_7(\text{OH})_2 \cdot 2\text{H}_2\text{O}$ precursor. Subsequently, $\text{ZrW}_{2-x}\text{Mo}_x\text{O}_7(\text{OH})_2 \cdot 2\text{H}_2\text{O}$ precursor powders were pre-calcined at 300–450 °C in an oven. About 2 g pre-calcined powders were loaded into graphite dies with an inner diameter of 10 mm and then pressed at an applied pressure of 50 MPa. The applied pressure was held constant until the end of the sintering period. The compacts were sintered at 500–600 °C for 10 min at 100 °C/min in argon atmosphere using an SPS apparatus (SPS-515S; Fuji Electronic Industrial, Saitama, Japan), with a pulse duration of 3.3 ms and on/off pulse intervals of 12:2 as recommended by the manufacturer. In this study, each sintered body was repetitively fabricated more than twice under the same conditions.

The relative densities of the $\text{ZrW}_{2-x}\text{Mo}_x\text{O}_8$ sintered bodies were measured using Archimedes' principle with distilled water. The density of distilled water is 0.99754 g/cm^3 at a room temperature of $23 \text{ }^\circ\text{C}$. The microstructural characteristics of the sintered bodies were examined with a scanning electron microscope (SEM) equipped with an X-ray energy-dispersive spectrometer (EDS) (JSM-IT100; JEOL, Tokyo, Japan). Phase identification was carried out using an X-ray powder diffraction (XRD) diffractometer (Ultima IV; Rigaku, Tokyo, Japan). The XRD measurements were carried out in a range of $10^\circ \leq 2\theta \leq 80^\circ$ at a scan speed of $6^\circ/\text{min}$, at $45 \text{ kV}/40 \text{ mA}$, and with $\text{Cu-K}\alpha$ radiation ($\lambda = 0.15406 \text{ nm}$). The NTE coefficients of the samples were measured with a thermodynamic analyzer (TMA-60/60H; Shimadzu, Kyoto, Japan). The data were collected at a heating rate of $1 \text{ }^\circ\text{C}/\text{min}$ from room temperature to $400 \text{ }^\circ\text{C}$.

To investigate the change in the phase transition temperature and NTE coefficient, high-temperature XRD (HT-XRD) experiments and Rietveld structure refinement were utilized. HT-XRD was performed using an X'Pert PRO X-ray diffractometer (Empyrean; PANalytical, Almelo, The Netherlands) with a semiconductor detector and a high-temperature attachment (HTK1200). Rietveld structure refinement was performed using General Structure Analysis System (GSAS) software (Los Alamos National Laboratory, Los Alamos, NM, USA) [25]. The Rietveld method was used at each temperature to refine the lattice parameter, the fractional coordinates, the overall temperature factor, the histogram scale factor, the background terms, and the pseudo-Voigt peak shape parameters. The visualization for electronic and structural analysis (VESTA) program was used for drawing the crystal structures [26].

3. Results and Discussion

3.1. Fabrication of Dense $\text{ZrW}_{2-x}\text{Mo}_x\text{O}_8$ Sintered Bodies

Figure 1a shows the XRD patterns of $\text{ZrW}_{2-x}\text{Mo}_x\text{O}_7(\text{OH})_2 \cdot 2\text{H}_2\text{O}$ ($x = 0, 1$) precursor powders prepared using only a sol-gel method. Although pure $\text{ZrW}_2\text{O}_7(\text{OH})_2 \cdot 2\text{H}_2\text{O}$ could be synthesized, $\text{ZrWMoO}_7(\text{OH})_2 \cdot 2\text{H}_2\text{O}$ could not be synthesized. The prepared powders were subjected to a hydrothermal process. As shown by the XRD results in Figure 1b, the precursors were well crystallized. They were indexed as pure $\text{ZrW}_2\text{O}_7(\text{OH})_2 \cdot 2\text{H}_2\text{O}$ and $\text{ZrWMoO}_7(\text{OH})_2 \cdot 2\text{H}_2\text{O}$. The fine precursor powders obtained using the sol-gel method combined with the hydrothermal process had higher crystallinity than those prepared using only the sol-gel method. Figure 1c shows the XRD patterns of the $\text{ZrW}_{2-x}\text{Mo}_x\text{O}_7(\text{OH})_2 \cdot 2\text{H}_2\text{O}$ ($0.0 \leq x \leq 1$) precursors. It can be observed that the precursors were well crystallized and were indexed as pure $\text{ZrW}_2\text{O}_7(\text{OH})_2 \cdot 2\text{H}_2\text{O}$ without any detectable impurities.

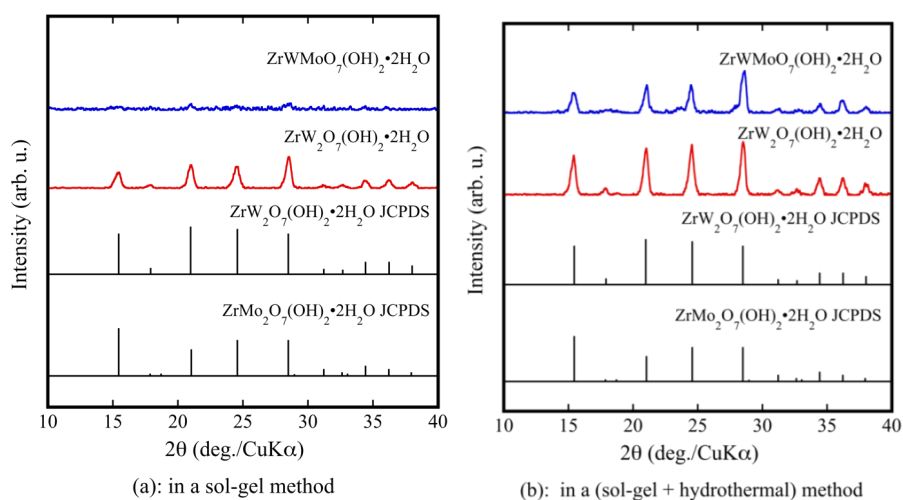


Figure 1. Cont.

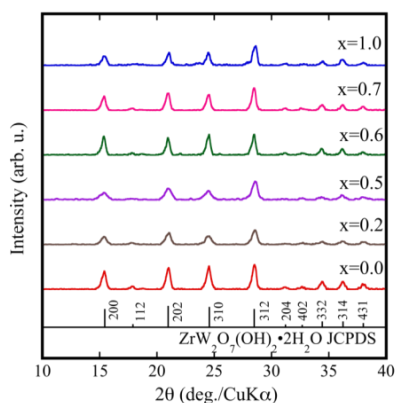
(c): $\text{ZrW}_{2-x}\text{Mo}_x\text{O}_7(\text{OH})_2 \cdot 2\text{H}_2\text{O}$ in a (sol-gel + hydrothermal) method

Figure 1. X-ray powder diffraction (XRD) patterns of $\text{ZrW}_{2-x}\text{Mo}_x\text{O}_7(\text{OH})_2 \cdot 2\text{H}_2\text{O}$ precursor powders in a sol-gel method (a); and a sol-gel method combines with hydrothermal method (b,c).

HT-XRD was performed to determine at which temperatures structural changes occur and to investigate the formation temperature of $\text{ZrW}_{2-x}\text{Mo}_x\text{O}_8$. Figure 2a shows the rising temperature results for the $\text{ZrW}_2\text{O}_7(\text{OH})_2 \cdot 2\text{H}_2\text{O}$ precursor powders. The precursor phase remained stable from room temperature to 100 °C. It can be observed that the crystalline precursors became amorphous at 200–500 °C. This change in the state is attributed to removal of the hydrate water in the crystalline precursor. High-temperature phase $\beta\text{-ZrW}_2\text{O}_8$ was obtained by heating at 550 °C. The $\beta\text{-ZrW}_2\text{O}_8$ was stable up to 630 °C; a small amount of WO_3 as an impurity was generated at temperatures above 630 °C. Figure 2b shows the falling temperature results. The peak intensities of the 111, 221, and 310 reflections increased as the temperature was reduced from 200 °C to 150 °C. The high-temperature β -phase changed to the low-temperature stable phase ($\alpha\text{-ZrW}_2\text{O}_8$). The 111, 221, and 310 reflections are attributed to the $\alpha\text{-ZrW}_2\text{O}_8$. The reflection peaks shifted to a higher angle (2θ degree) as the temperature was reduced, meaning that the volume of material expanded during cooling.

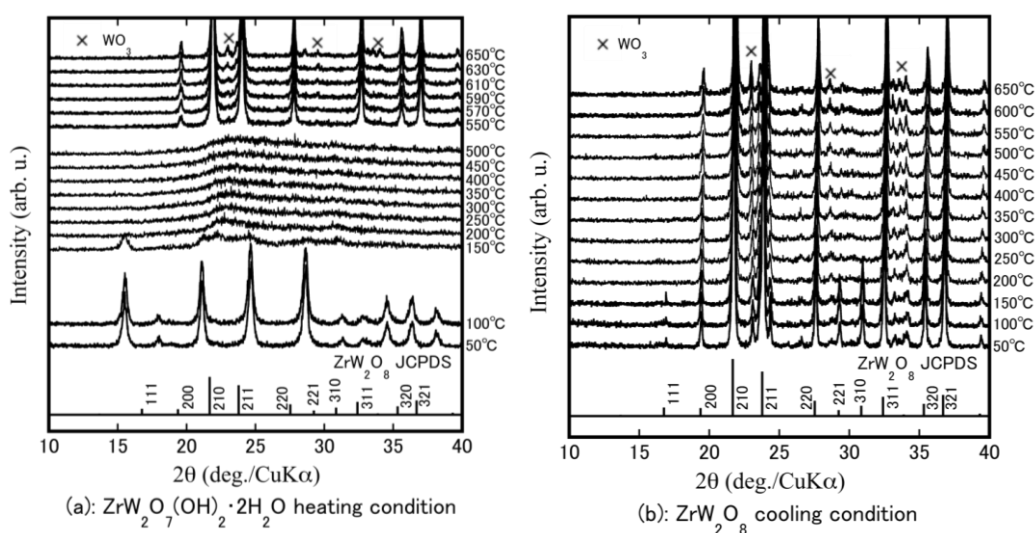


Figure 2. High temperature (HT)-XRD patterns of Zr–W–O system precursor at a temperature program of heating from 50 °C to 650 °C (a); and then cooling from 650 °C to 50 °C (b).

Using the results shown in Figure 2a, we performed multiple temperature comparison experiments to fabricate $\text{ZrW}_{2-x}\text{Mo}_x\text{O}_8$ sintered bodies by SPS. The optimum sintering temperature for each sample depended on various factors (relative density, crystallinity, etc.). Figure 3 shows the

XRD patterns for each $\text{ZrW}_{2-x}\text{Mo}_x\text{O}_8$ sintered body under optimal sintering temperature conditions. The optimal sintering temperature depended on the Mo content: 600 °C for $x = 0.0$, 550 °C for $x = 0.5$, and 500 °C for $x = 1.0$. The $\text{ZrW}_{2-x}\text{Mo}_x\text{O}_8$ sintered bodies were pure phase and consistent with ZrW_2O_8 . The 111, 221, and 310 reflections progressively diminished with increasing Mo substitution and almost disappeared when $x \geq 0.7$. The reflection intensity decreased in the order of 111, 221, and 310 in accordance with the generation of β phase and substitution of W by Mo. These results suggest that the crystal phase of the $\text{ZrW}_{2-x}\text{Mo}_x\text{O}_8$ compound depends on the x value. When x was increased to 0.7 at room temperature, $\text{ZrW}_{2-x}\text{Mo}_x\text{O}_8$ completely converted to the β phase. The density of the obtained $\text{ZrW}_{2-x}\text{Mo}_x\text{O}_8$ sintered bodies and theoretical density are shown in Table 1. All sintered bodies with relative densities of more than 90% were obtained with a shorter heat treatment compared with the conventional sintering process. Thus, SPS is a promising method for densification of body structures as it promotes fast heating and fast cooling of sintered bodies.

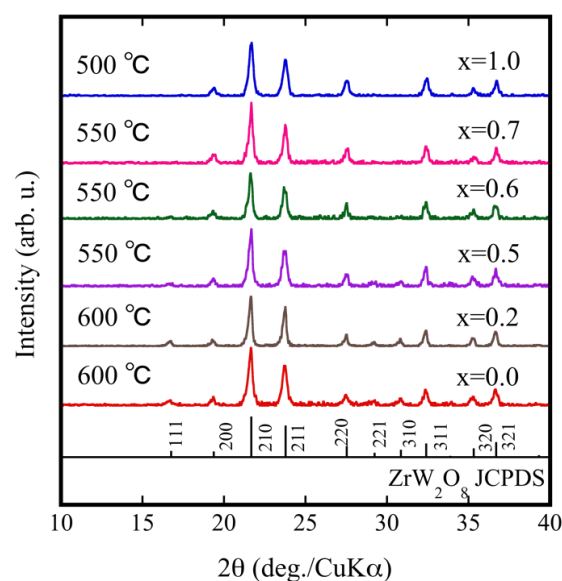


Figure 3. XRD patterns of $\text{ZrW}_{2-x}\text{Mo}_x\text{O}_8$ sintered bodies.

Table 1. Measurement density and relative densities of $\text{ZrW}_{2-x}\text{Mo}_x\text{O}_8$ sintered bodies.

| Compound | $x = 0.0$ | $x = 0.2$ | $x = 0.5$ | $x = 0.6$ | $x = 0.7$ | $x = 1.0$ |
|--|-----------|-----------|-----------|-----------|-----------|-----------|
| Sintering temperature (°C) | 600 | 600 | 550 | 550 | 550 | 500 |
| Density (g/cm^3) | 4.6271 | 4.6832 | 4.4217 | 4.4855 | 4.2760 | 4.1689 |
| Theoretical density (g/cm^3) | 5.08 | 4.93 | 4.71 | 4.63 | 4.56 | 4.33 |
| Relative density (%) | 91.0846 | 94.9939 | 93.8790 | 96.8790 | 93.7719 | 96.2794 |

Figure 4 shows SEM images of the fractured surface of the sintered body. The SEM image shows that the sintered body was very dense. This is attributed to the applied pressure during SPS, which enhanced densification over grain-growth-promoting diffusion mechanisms. In addition, EDS point analysis of the fractured surface was performed to determine the composition of the black areas. A comparison of the elemental compositions of the black and bright areas revealed no significant change in the Zr, W, and O contents, indicating that the black areas were not impure substances.

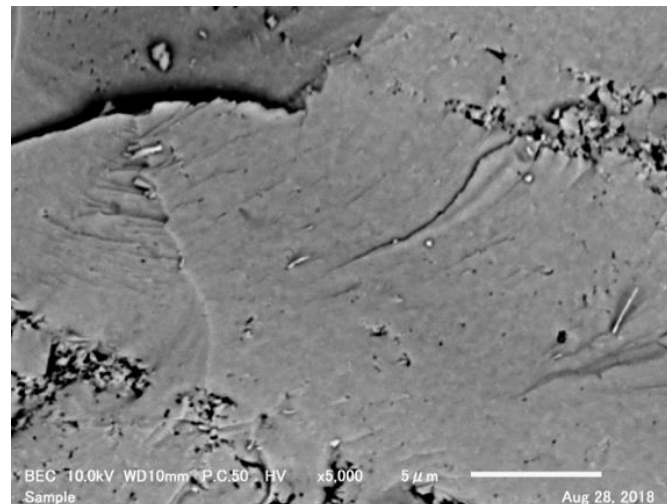


Figure 4. Scanning electron microscope (SEM) image of fractured surface of ZrW_2O_8 sintered body.

3.2. Evaluation of Thermal Expansion Properties of $ZrW_{2-x}Mo_xO_8$ Sintered Bodies

For the α - $ZrW_{2-x}Mo_xO_8$, the 111 reflection in the vicinity of 17° and the 221 and 310 reflections around 30° were clearly observed at room temperature. In contrast, for the β - $ZrW_{2-x}Mo_xO_8$, there were no reflections around 17° and 30° . Therefore, because of the existence of the 111, 221, and 310 reflections in the X-ray diffraction pattern, the phase transition temperature could be calculated from α phase to β phase from the high-temperature X-ray diffraction patterns (Figure 5). The phase transition temperature of ZrW_2O_8 corresponded to the previously reported temperature (around 160°C – 170°C), that for $x = 0.2$ was slightly lower (140°C – 150°C), and that for $x = 0.5$ was 70°C – 80°C . These findings show that the phase transition temperature of $ZrW_{2-x}Mo_xO_8$ decreases with increasing Mo substitution. The disappearance of the 111, 221, and 310 reflections in the XRD pattern of $ZrWMoO_8$ indicates that $ZrWMoO_8$ exists in the β phase above room temperature.

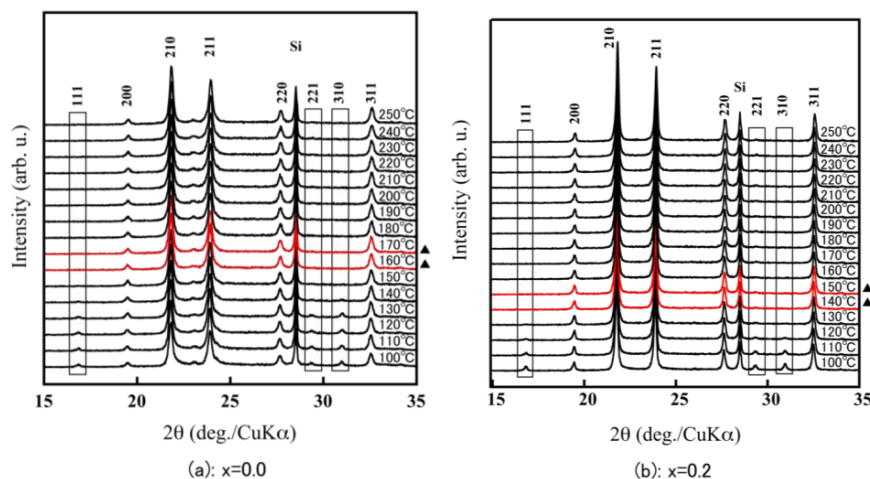


Figure 5. Cont.

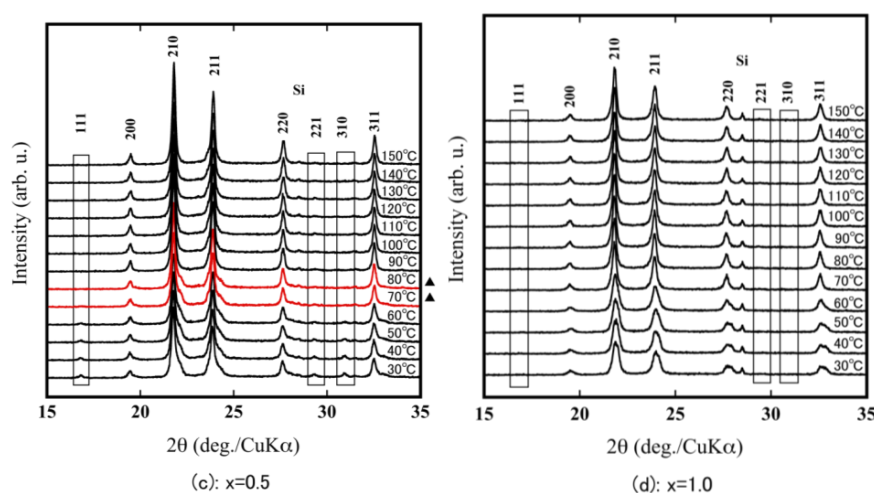


Figure 5. HT-XRD patterns of $ZrW_{2-x}Mo_xO_8$ sintered bodies (a): $x = 0.0$; (b): $x = 0.2$; (c): $x = 0.5$; (d): $x = 1.0$; (▲: phase transition interval).

To investigate and identify the effect of Mo doping on the phase transition temperature and on the NTE coefficients, we measured the relative thermal expansion of $ZrW_{2-x}Mo_xO_8$ sintered bodies as a function of temperature. The results are shown in Figure 6. The downward trend of each curve with increasing temperature reflects the NTE property. The bending point in each curve is attributed to a change in the NTE coefficient, which corresponds to the occurrence of phase transitions in this study. These results show that the phase transition shifts to the lower temperature side as the Mo content is increased. The phase transition from α -phase to β -phase could be investigated when $x \leq 0.6$, but not when $0.7 \leq x$ within the measurement temperature range. The decrease in the phase transition temperature is attributed to the fact that the electronegativity of Mo (2.16) is less than that of W (2.36). This means that when the Mo content is gradually increased, the separation energy of W(Mo)–O gradually decreases, leading to a reduction in the phase transition temperature.

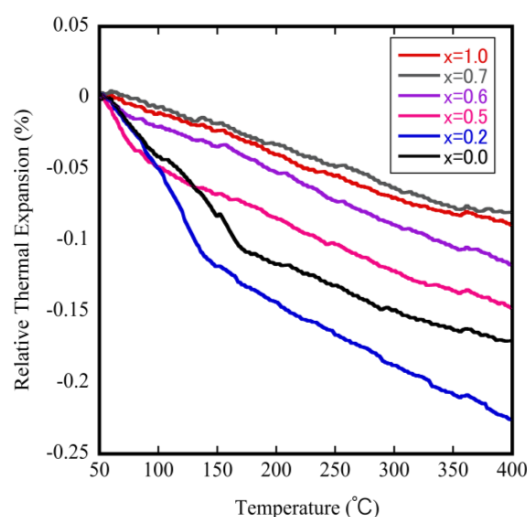


Figure 6. Thermodynamic analyzer (TMA) results for $ZrW_{2-x}Mo_xO_8$ sintered bodies.

The NTE coefficient can be automatically calculated from the change in the dimensions of the material with temperature. The values for the $ZrW_{2-x}Mo_xO_8$ samples are shown in Table 2. All samples showed the NTE property: the NTE coefficient can be controlled by changing the x value as follows: from $-7.85 \times 10^{-6} \text{ } ^\circ\text{C}^{-1}$ ($x = 0$) to $-9.01 \times 10^{-6} \text{ } ^\circ\text{C}^{-1}$ ($x = 0.6$) and from $-3.22 \times 10^{-6} \text{ } ^\circ\text{C}^{-1}$ ($x = 0$) to

$-2.50 \times 10^{-6} \text{ }^\circ\text{C}^{-1}$ ($x = 1.0$) before and after the phase transition, respectively. The NTE coefficients of the β phase decreased as more Mo was substituted. The reason for this phenomenon will be discussed below.

Table 2. Negative thermal expansion (NTE) and phase transition temperature for $\text{ZrW}_{2-x}\text{Mo}_x\text{O}_8$ sintered bodies (50–400 °C) by thermodynamic analyzer (TMA).

| Compound | Coefficient of Thermal Expansion ($\times 10^{-6} \text{ }^\circ\text{C}^{-1}$) | | Phase Transition Temperature (°C) |
|-----------|---|--------------------|-----------------------------------|
| | α Phase | β Phase | |
| $x = 0.0$ | −7.85 (50–130 °C) | −3.22 (200–400 °C) | 170 |
| $x = 0.2$ | −11.79 (50–130 °C) | −4.17 (200–400 °C) | 145 |
| $x = 0.5$ | −15.34 (50–70 °C) | −3.16 (200–400 °C) | 78 |
| $x = 0.6$ | −9.01 (50–70 °C) | −3.21 (200–400 °C) | 60 |
| $x = 0.7$ | - | −2.91 (200–400 °C) | - |
| $x = 1.0$ | - | −2.50 (200–400 °C) | - |

3.3. Rietveld Structure Refinement of $\text{ZrW}_{2-x}\text{Mo}_x\text{O}_8$ Compounds

Crystal structures of undoped and Mo-substituted ZrW_2O_8 (ZrW_2O_8 , $\text{ZrW}_{1.8}\text{Mo}_{0.2}\text{O}_8$, $\text{ZrW}_{1.5}\text{Mo}_{0.5}\text{O}_8$) compounds were generated using refined lattice parameters and atomic coordinates at room temperature, 100 °C, 150 °C, 200 °C, 250 °C, and 300 °C. The structural parameters obtained from Rietveld refinement of these samples at room temperature and 300 °C are listed in Table 3. Comparison of these samples revealed no obvious changes in the fractional coordinates with changes in the temperature or Mo content, indicating that the addition of Mo does not change the original structure of ZrW_2O_8 .

Figures 7 and 8a,b shown the refinement results and corresponding crystal structures of ZrW_2O_8 at room temperature for α phase and at 300 °C for β phase. The crystal structures contain corner-sharing ZrO_6 octahedra and WO_4 tetrahedra. The ZrO_6 octahedra share all six corners with the WO_4 tetrahedra, whereas the WO_4 tetrahedra share only three of their four corners with the ZrO_6 octahedra. In other words, each WO_4 tetrahedron has one coordination oxygen atom, which is called ‘terminal’ oxygen. (In this study, O4 and O3 correspond to the terminal oxygen in the W1O_4 and W2O_4 tetrahedra, respectively). The NTE property of both phases of the ZrW_2O_8 can be simply defined as follows: the WO_4 polyhedra rotate inward as the temperature rises, and the ZrO_6 octahedra stretch to shrink the decrease in volume due to this rotation². The only structural difference between the α and β phases is in the W1O_4 and W2O_4 tetrahedra. A view of the WO_4 groups in the $\langle 111 \rangle$ direction of ZrW_2O_8 at RT and 300 °C is shown in Figure 8c,d. The WO_4 tetrahedra are arranged in pairs along the main three-fold axis of the cubic unit cell, forming condensed W_2O_8 units. The ‘terminal’ O atom of each WO_4 tetrahedron points in the same direction in the W_2O_8 unit, leading to an O4–W1...O3–W2 arrangement. In the α phase structure, the two WO_4 tetrahedra are not bound together at a certain distance. In comparison, the inversion of W1O_4 and W2O_4 tetrahedra is arranged in pairs, forming condensed W_2O_8 polyhedra when the phase transition occurs.

Table 3. Rietveld refinement of atomic coordinates and occupancy of $\text{ZrW}_{2-x}\text{Mo}_x\text{O}_8$.

| Temperature | Room Temperature | | | 300 °C | | |
|------------------------------|--------------------------|---|---|--------------------------|---|---|
| Compound | ZrW_2O_8 | $\text{ZrW}_{1.8}\text{Mo}_{0.2}\text{O}_8$ | $\text{ZrW}_{1.5}\text{Mo}_{0.5}\text{O}_8$ | ZrW_2O_8 | $\text{ZrW}_{1.8}\text{Mo}_{0.2}\text{O}_8$ | $\text{ZrW}_{1.5}\text{Mo}_{0.5}\text{O}_8$ |
| Goodness-of-fit (χ^2) | 1.776 | 6.993 | 3.983 | 1.375 | 2.928 | 3.194 |
| Space Group | $P 2_1 3$ | $P 2_1 3$ | $P 2_1 3$ | $P a \bar{3}$ | $P a \bar{3}$ | $P a \bar{3}$ |
| Atom | Zr | Zr | Zr | Zr | Zr | Zr |
| $x = y = z$ | 0.000319 | 0.004534 | 0.002891 | 0.000000 | 0.000000 | 0.000000 |
| Occupancy | 1 | 1 | 1 | 1 | 1 | 1 |
| Atom | W1 | W(Mo)1 | W(Mo)1 | W1 | W(Mo)1 | W(Mo)1 |
| $x = y = z$ | 0.342614 | 0.343947 | 0.351651 | 0.340273 | 0.339711 | 0.338886 |
| Occupancy | 1 | W1:0.9, Mo1:0.1 | W1:0.75, Mo1:0.25 | 0.5 | W1:0.45, Mo1:0.05 | W1:0.375, Mo1:0.125 |

Table 3. Cont.

| Temperature | Room Temperature | | | 300 °C | | |
|-------------|------------------|-----------------|-------------------|-----------|-------------------|---------------------|
| Atom | W2 | W(Mo)2 | W(Mo)2 | W2 | W(Mo)2 | W(Mo)2 |
| $x = y = z$ | 0.601688 | 0.603332 | 0.608726 | 0.603304 | 0.605205 | 0.606212 |
| Occupancy | 1 | W2:0.9, Mo2:0.1 | W2:0.75, Mo2:0.25 | 0.5 | W2:0.45, Mo2:0.05 | W2:0.375, Mo2:0.125 |
| Atom | O1 | O1 | O1 | O1 | O1 | O1 |
| x | 0.042345 | 0.021103 | 0.008577 | 0.050445 | 0.055887 | 0.05519 |
| y | -0.19759 | -0.179137 | -0.183323 | -0.205553 | -0.201601 | -0.202851 |
| z | -0.058376 | -0.066893 | -0.057469 | -0.069239 | -0.073105 | -0.0735229 |
| Occupancy | 1 | 1 | 1 | 1 | 1 | 1 |
| Atom | O2 | O2 | O2 | - | - | - |
| x | 0.078837 | 0.094246 | 0.121337 | - | - | - |
| y | -0.057928 | -0.071485 | -0.094012 | - | - | - |
| z | 0.211437 | 0.221976 | 0.205825 | - | - | - |
| Occupancy | 1 | 1 | 1 | - | - | - |
| Atom | O3 | O3 | O3 | O3 | O3 | O3 |
| $x = y = z$ | 0.486051 | 0.479937 | 0.469176 | 0.509573 | 0.510211 | 0.512884 |
| Occupancy | 1 | 1 | 1 | 0.5 | 0.5 | 0.5 |
| Atom | O4 | O4 | O4 | O4 | O4 | O4 |
| $x = y = z$ | 0.250373 | 0.262464 | 0.262221 | 0.231004 | 0.228680 | 0.231430 |
| Occupancy | 1 | 1 | 1 | 0.5 | 0.5 | 0.5 |

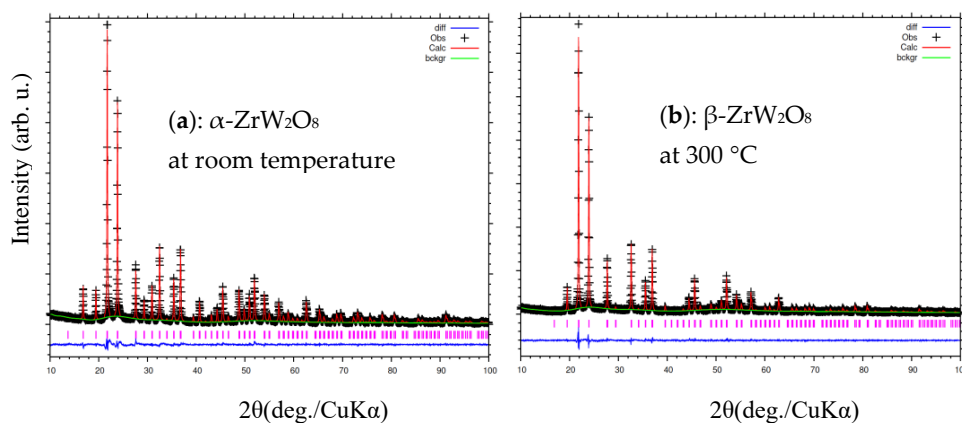


Figure 7. Rietveld refinement of X-ray diffraction patterns of ZrW₂O₈ at (a) room temperature; and (b) 300 °C.

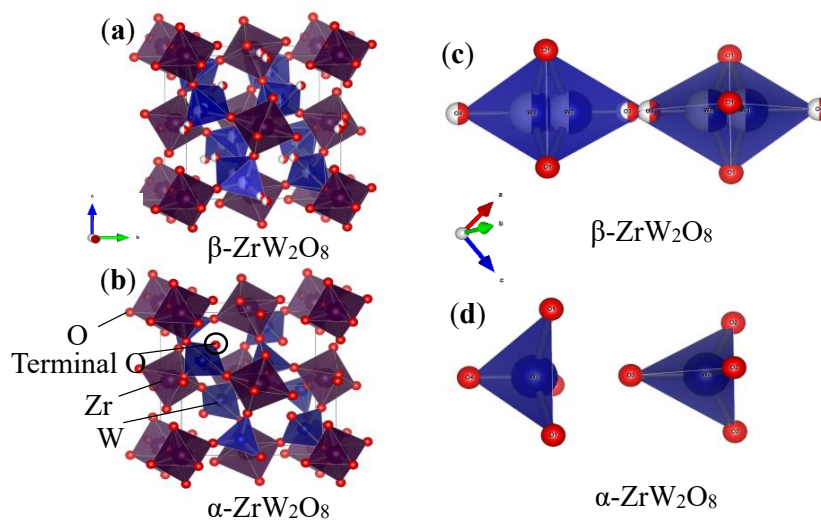


Figure 8. Crystal structure of (a) α phase and (b) β phase of ZrW₂O₈; WO₄ groups in <111> direction of (c) α phase and (d) β phase of ZrW₂O₈.

The temperature dependence of the lattice parameters on the Mo content derived from Rietveld refinement is shown in Figure 9. The lattice parameter for these samples clearly decreased with the increase in Mo content at the same temperature, which is reasonable given the smaller radius of Mo^{6+} (0.41 Å) compared with that of W^{6+} (0.42 Å). In addition, the lattice parameters of all samples contracted linearly with increasing temperature, indicating that the thermal expansion behavior is negative. The coefficient of thermal expansion calculated on the basis of the relationship between the temperature and lattice parameters is shown in Table 4. The NTE coefficients changed from $-9.88 \times 10^{-6} \text{ }^\circ\text{C}^{-1}$ to $-5.35 \times 10^{-6} \text{ }^\circ\text{C}^{-1}$ for ZrW_2O_8 . The reduction in the β phase with the addition of Mo content is consistent with the decreasing trends of the TMA results (Table 2). We compared the NTE coefficients in Tables 2 and 4 and found that the results of the two measurements differed. The reason for this difference is attributed to two factors. The first one is the presence of pores inside the sintered body, which could be roughly observed by SEM. The second one is the presence of systematic errors due to the use of different instruments, temperature controllers, and high-temperature furnaces.

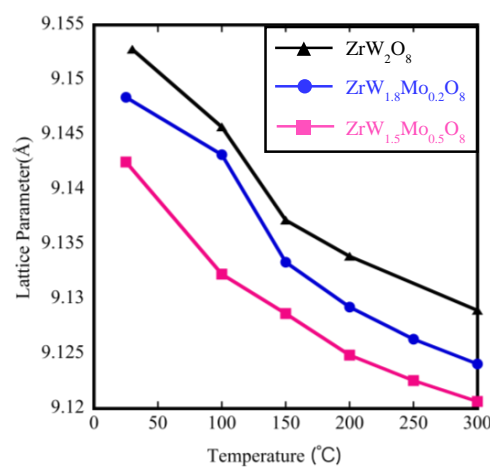


Figure 9. Lattice parameters of $\text{ZrW}_{2-x}\text{Mo}_x\text{O}_8$.

Table 4. High temperature (HT)-X-ray powder diffraction (XRD) calculated NTE coefficients for $\text{ZrW}_{2-x}\text{Mo}_x\text{O}_8$.

| Compound | Calculated Coefficient of Thermal Expansion by Lattice Parameter ($\times 10^{-6} \text{ }^\circ\text{C}^{-1}$) | |
|---|---|---------------|
| | α Phase | β Phase |
| ZrW_2O_8 | -9.88 | -5.35 |
| $\text{ZrW}_{1.8}\text{Mo}_{0.2}\text{O}_8$ | -7.4 | -4.72 |
| $\text{ZrW}_{1.5}\text{Mo}_{0.5}\text{O}_8$ | - | -3.95 |

To intuitively investigate the mechanism of the reduction in the NTE coefficients in the β phase with an increase in Mo content, we examined the variations in bond length, bond angle, and distortion of ZrO_6 and WO_4 polyhedra. The bond lengths and angles of ZrO_6 and WO_4 polyhedra for all samples at 200 °C and 300 °C are shown in Figures 10 and 11. For the ZrO_6 octahedra, the Zr–O1 bond lengths in each polyhedron are equal, and the Mn–O bond length is close to the sum of the ionic radii ($r_{\text{Zr}} + r_{\text{O}} = 2.07 \text{ Å}$). The variations in bond length were minor; the lengths varied from 2.01 Å to 2.04 Å with changes in the Mo content. The bond angles of O1–Zr–O1 exhibited minor deviations from the octahedral symmetry, while the bond angle of O1–Zr–O1 remained constant at around 90°, indicating that the ZrO_6 octahedra in all samples were close to a regular octahedron. This means that the ZrO_6 octahedra in all samples resembled a rigid body.

Compared with the rigid ZrO_6 octahedra, the $\text{W}(\text{Mo})_2\text{O}_8$ polyhedra appear to be distorted to a large extent. In these compounds, there were three identical $\text{W}(\text{Mo})1\text{--O}1$ bonds and three identical $\text{W}(\text{Mo})2\text{--O}1$ bonds, while the $\text{W}1\text{--O}4$ and $\text{W}2\text{--O}3$ bonds existed alone. The angles of each bond in

the $W(Mo)_2O_8$ polyhedra did not change with a change in Mo content—they were basically fixed at $116(1)^\circ$ for O1–W(Mo)1–O1, $109(1)^\circ$ for O1–W(Mo)2–O1, $99(2)^\circ$ for O1–W(Mo)1–O4, and $108(1)^\circ$ for O1–W(Mo)2–O3. The bond lengths for W(Mo)1–O1 decreased with an increase in Mo content, which may be related to the fact that the ionic radius of Mo^{6+} is less than that of W^{6+} .

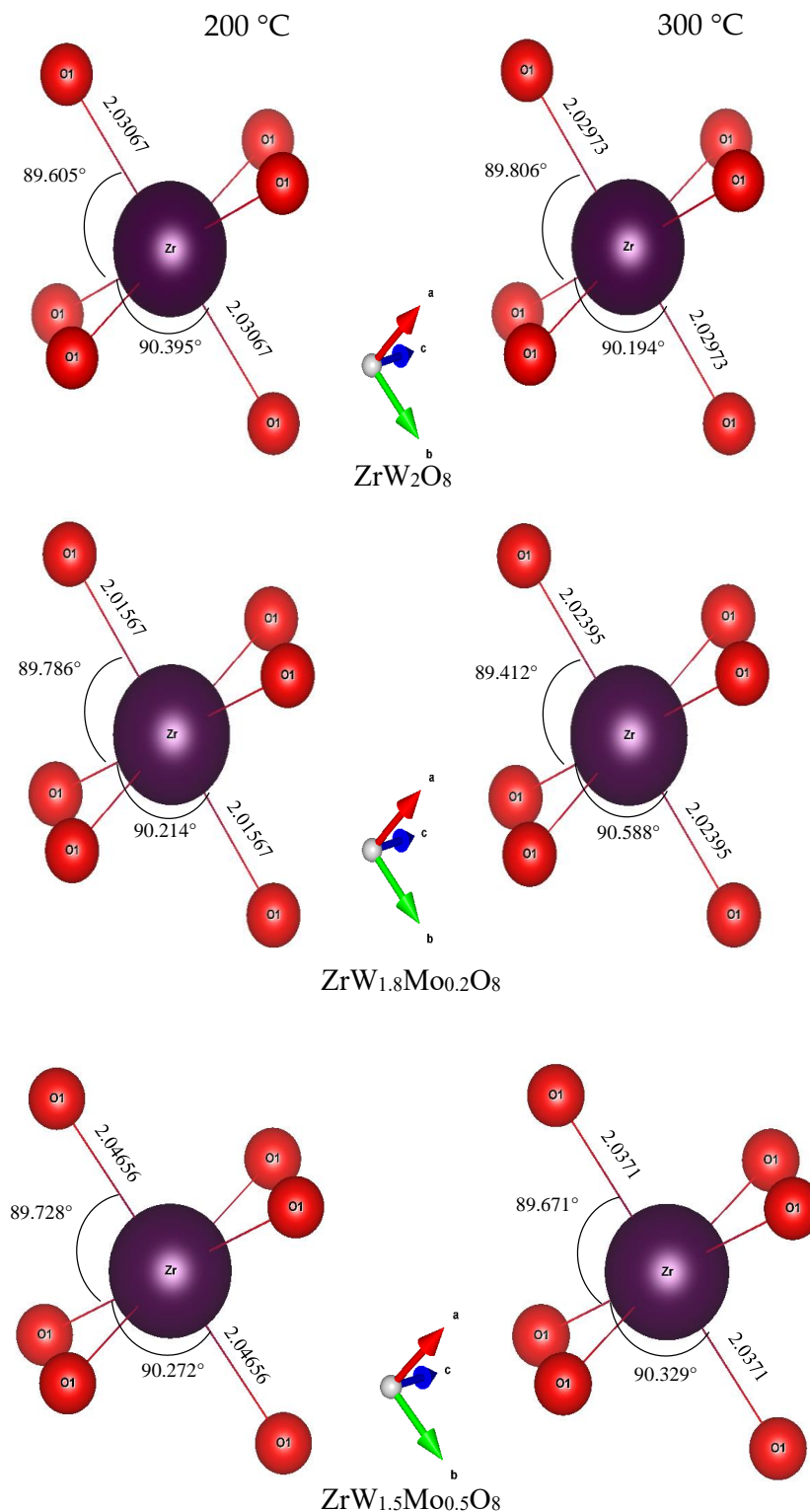


Figure 10. Bond lengths and bond angles of ZrO_6 octahedron in $ZrW_{2-x}Mo_xO_8$ compounds.

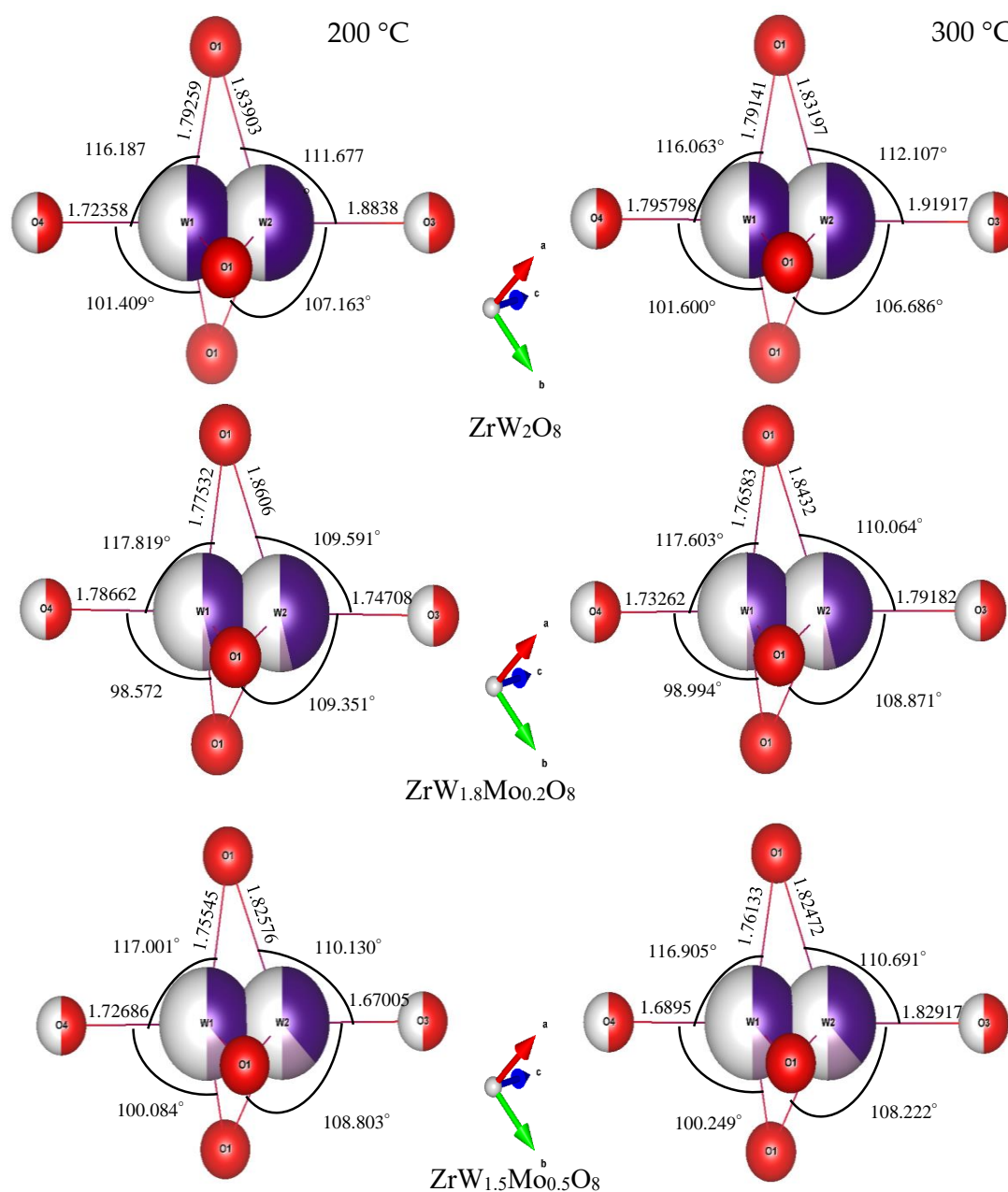


Figure 11. Bond lengths and bond angles of $W(Mo)_2O_8$ polyhedra in $ZrW_{2-x}Mo_xO_8$ compounds.

A noteworthy finding is that the bond lengths of $W(Mo)1-O_4$ and $W(Mo)2-O_3$ not only varied greatly with the temperature (from 200 °C to 300 °C), but also varied greatly with the Mo content. This may be related to the one-coordination of O_3 and O_4 atoms. Different $W(Mo)-O$ bond lengths in different directions indicate stronger distortion in the polyhedra. Two factors necessary for distortion of a polyhedron are quadratic elongation (λ) and bond angle variance (σ^2) [27]. The variance values of the distortion constants λ and σ^2 between 200 °C and 300 °C are shown in Figure 12. We can see that the ZrO_6 octahedron is basically in an undistorted state, which is attributed to all bond lengths $Zr-O_1$ being equal and all bond angles being close to 90°. In the $W(Mo)_2O_8$ polyhedron, the degree of distortion increased greatly with the temperature because of the instability of the one-coordinate oxygen atoms. The degree of distortion gradually decreased with increasing Mo content, resulting in a decrease in the NTE coefficient.

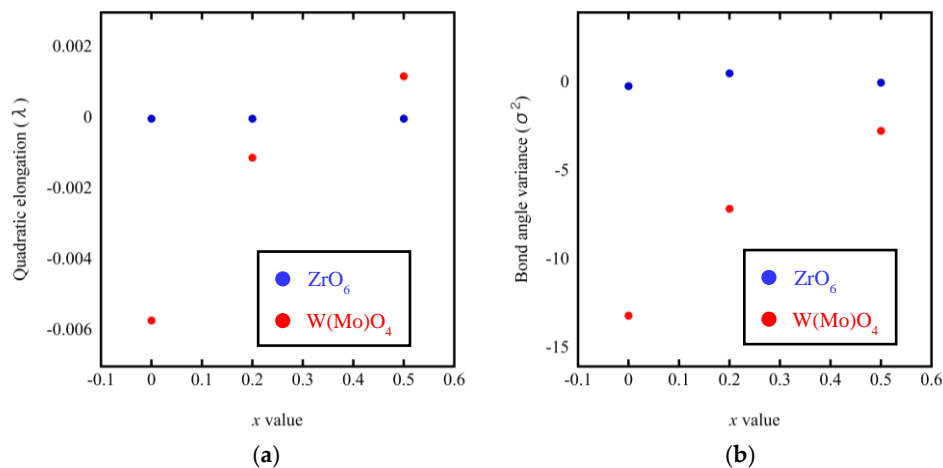


Figure 12. Quadratic elongation (a) and bond angle variance (b) of ZrO₆ and W(Mo)₂O₈ polyhedra in ZrW_{2-x}Mo_xO₈.

4. Conclusions

Single-phase ZrW_{2-x}Mo_xO₈ ($0 \leq x \leq 1$) sintered bodies with a relative density greater than 90% were obtained by spark plasma sintering using ZrW_{2-x}Mo_xO₇(OH)₂·2H₂O precursor powders as the starting material and a relatively low-temperature heat treatment (500 °C–600 °C). The α - β phase transition temperature of the ZrW_{2-x}Mo_xO₈ sintered bodies decreased as more Mo was substituted at W sites. When $x \geq 0.7$, the α - β phase transition could not be observed above room temperature. The coefficient of negative thermal expansion of ZrW_{2-x}Mo_xO₈ can be controlled by changing the amount of Mo substituted at W sites. These single ZrW_{2-x}Mo_xO₈ ($0 \leq x \leq 1$) sintered bodies with a controllable coefficient of negative thermal expansion have a wide range of applications.

Author Contributions: H.W. and M.H. conceived and designed the experiments; H.W., M.H., and S.M. performed the experiments; A.A. and K.F. contributed analysis tools; H.W. and K.N. analyzed and interpreted the experimental data; H.W. wrote the paper; K.N. revised the manuscript for publication.

Funding: This research received no external funding.

Conflicts of Interest: The authors declare no conflict of interest.

References

- Ouyang, J.S.; Li, Y.B.; Chen, B.; Huang, D.H. Macro-Scale Strength and Microstructure of ZrW₂O₈ Cementitious Composites with Tunable Low Thermal Expansion. *Materials* **2018**, *11*, 748. [[CrossRef](#)] [[PubMed](#)]
- Holzer, H.; Dunand, D.C. Phase Transformation and Thermal Expansion of Cu/ZrW₂O₈ Metal Matrix Composites. *J. Mater. Res.* **1999**, *14*, 780–789. [[CrossRef](#)]
- Wu, Y.; Wang, M.L.; Chen, Z.; Ma, N.H.; Wang, H.W. The effect of phase transformation on the thermal expansion property in Al/ZrW₂O₈ composites. *J. Mater. Sci.* **2013**, *48*, 2928–2933. [[CrossRef](#)]
- Kanamori, K.; Kineri, T.; Fukuda, R.; Kawano, T.; Nishio, K. Low-temperature sintering of ZrW₂O₈-SiO₂ by spark plasma sintering. *J. Mater. Sci.* **2009**, *44*, 855–860. [[CrossRef](#)]
- Wu, G.; Zhou, C.; Zhang, Q.; Pei, R. Decomposition of ZrW₂O₈ in Al matrix and the influence of heat treatment on ZrW₂O₈/Al-Si thermal expansion. *Scr. Mater.* **2015**, *96*, 29–32. [[CrossRef](#)]
- Yilmaz, S. Thermal mismatch stress development in Cu-ZrW₂O₈ composite investigated by synchrotron X-ray diffraction. *Compos. Sci. Technol.* **2002**, *62*, 1835–1839. [[CrossRef](#)]
- Mary, T.A.; Evans, J.S.O.; Vogt, T.; Sleight, A.W. Negative thermal expansion from 0.3 to 1050 Kelvin in ZrW₂O₈. *Science* **1996**, *272*, 90–92. [[CrossRef](#)]
- Evans, J.S.O.; Mary, T.A.; Vogt, T.; Subramanian, M.A.; Sleight, A.W. Negative Thermal Expansion in ZrW₂O₈ and HfW₂O₈. *Chem. Mater.* **1996**, *8*, 2809–2823. [[CrossRef](#)]

9. Evans, J.S.O.; David, W.I.F.; Sleight, A.W. Structural investigation of the negative-thermal-expansion material ZrW_2O_8 . *Acta Crystallogr. B* **1999**, *55*, 333–340. [[CrossRef](#)] [[PubMed](#)]
10. Meyer, C.D.; Bouree, F.; Evans, J.S.O.; Buysse, K.D.; Bruneel, E.; Driessche, I.V.; Hoste, S. Structure and phase transition of Sn-substituted $Zr_{(1-x)}Sn_xW_2O_8$. *J. Mater. Chem.* **2004**, *14*, 2988–2994. [[CrossRef](#)]
11. Evans, J.S.O.; Hanson, P.A.; Ibberson, R.M.; Kameswari, U.; Duan, N.; Sleight, A.W. Low-Temperature Oxygen Migration and Negative Thermal Expansion in $ZrW_{2-x}Mo_xO_8$. *J. Am. Chem. Soc.* **2000**, *122*, 8694–8699. [[CrossRef](#)]
12. Korthuis, V.; Khosrovani, N.; Sleight, A.W.; Roberts, N.; Dupree, R.; Warren, W.W. Negative Thermal Expansion and Phase Transitions in the $ZrV_{2-x}P_xO_7$ Series. *Chem. Mater.* **1995**, *7*, 412–417. [[CrossRef](#)]
13. Khosrovani, N.; Korthuis, V.; Sleight, A.W.; Vogt, T. Unusual 180° P–O–P Bond Angles in ZrP_2O_7 . *Inorg. Chem.* **1996**, *35*, 485–489. [[CrossRef](#)] [[PubMed](#)]
14. Evans, J.S.O.; Hanson, J.C.; Sleight, A.W. Room-Temperature Superstructure of ZrV_2O_7 . *Acta. Cryst.* **1998**, *B54*, 705–713. [[CrossRef](#)]
15. Turquat, C.; Muller, C.; Nigrelli, E.; Leroux, C.; Soubeyroux, J.L.; Nihoul, G. Structural investigation of temperature-induced phase transitions in HfV_2O_7 . *Eur. Phys. J. Appl. Phys.* **2000**, *10*, 15–27. [[CrossRef](#)]
16. Huang, C.H.; Knop, O.; Othen, D.A.; Woodhams, F.W.D.; Howie, R.A. Pyrophosphates of Tetravalent Elements and a Mössbauer Study of SnP_2O_7 . *Can. J. Chem.* **1975**, *53*, 79–91. [[CrossRef](#)]
17. Evans, J.S.O.; Mary, T.A. Structural phase transitions and negative thermal expansion in $Sc_2(MoO_4)_3$. *Int. J. Inorg. Mater.* **2000**, *2*, 143–151. [[CrossRef](#)]
18. Abrahams, S.C.; Bernstein, J.L. Crystal Structure of the Transition-Metal Molybdates and Tungstates. II. Diamagnetic $SC_2(WO_4)_3$. *J. Chem. Phys.* **1966**, *45*, 2745–2752. [[CrossRef](#)]
19. Gates, S.D.; Colin, J.A.; Lind, C. Non-hydrolytic sol-gel synthesis, properties, and high-pressure behavior of gallium molybdate. *J. Mater. Chem.* **2006**, *16*, 4214–4219. [[CrossRef](#)]
20. Allen, S.; Evans, J.S.O. Negative thermal expansion and oxygen disorder in cubic $ZrMo_2O_8$. *Phys. Rev. B* **2003**, *68*, 134101–134103. [[CrossRef](#)]
21. Ahmad, M.I.; Lindley, K.; Akinc, M. Hydrothermal Synthesis of $ZrW_{2-\delta}Mo_\delta O_8$ ($\delta = 0-0.91$) and its $\alpha \rightarrow \beta$ Transformation. *J. Am. Ceram. Soc.* **2011**, *94*, 2619–2624. [[CrossRef](#)]
22. Zhao, R.Q.; Yang, X.J.; Wang, H.L.; Han, J.S.; Ma, H.; Zhao, X. A novel route to synthesize cubic $ZrW_{2-x}Mo_xO_8$ ($x = 0-1.3$) solid solutions and their negative thermal expansion properties. *J. Solid State Chem.* **2007**, *180*, 3160–3165. [[CrossRef](#)]
23. Huang, L.; Xiao, Q.G.; Ma, H.; Li, G.B.; Liao, F.H.; Qi, C.M.; Zhao, X.H. Phase Behaviors of the $ZrMo_{2-x}W_xO_8$ ($x = 0.2-2.0$) System and the Preparation of an Mo-Rich Cubic Phase. *Eur. J. Inorg. Chem.* **2005**, *2005*, 4521–4526. [[CrossRef](#)]
24. Kanamori, K.; Kineri, T.; Fukuda, R.; Nishio, K.; Hashimoto, M.; Mae, H. Spark Plasma Sintering of Sol-Gel Derived Amorphous ZrW_2O_8 Nanopowder. *J. Am. Ceram. Soc.* **2009**, *92*, 32–35. [[CrossRef](#)]
25. Larson, A.C.; Von Dreele, R.B.; Alamos, L. *General Structural Analysis System (GSAS)*; Los Alamos National Laboratory Report LAUR; Los Alamos National Laboratory: Los Alamos, NM, USA, 2000.
26. Momma, K.; Izumi, F. VESTA 3 for three-dimensional visualization of crystal, volumetric and morphology data. *J. Appl. Crystallogr.* **2011**, *44*, 1272–1276. [[CrossRef](#)]
27. Robinson, K.; Gibbs, G.V.; Ribbe, P.H. Quadratic elongation: A quantitative measure of distortion in coordination polyhedra. *Science* **1971**, *172*, 567–570. [[CrossRef](#)] [[PubMed](#)]

